

# Vibronic states and their effect on the temperature and strain dependence of silicon-vacancy qubits in 4H silicon carbide

Péter Udvarhelyi,<sup>1,2,3</sup> Gergő Thiering,<sup>2</sup> Naoya Morioka,<sup>4</sup> Charles Babin,<sup>4</sup> Florian Kaiser,<sup>4</sup> Daniil Lukin,<sup>5</sup> Takeshi Ohshima,<sup>6</sup> Jawad Ul-Hassan,<sup>7</sup> Nguyen Tien Son,<sup>7</sup> Jelena Vučković,<sup>5</sup> Jörg Wrachtrup,<sup>4</sup> and Adam Gali<sup>2,3</sup>

<sup>1</sup>*Department of Biological Physics, Eötvös University,  
Pázmány Péter sétány 1/A, H-1117 Budapest, Hungary*

<sup>2</sup>*Wigner Research Centre for Physics, P.O. Box 49, H-1525 Budapest, Hungary*

<sup>3</sup>*Department of Atomic Physics, Budapest University of Technology and Economics, Budafoki út 8., H-1111 Budapest, Hungary*

<sup>4</sup>*3rd Institute of Physics, University of Stuttgart and Institute for  
Quantum Science and Technology IQST, 70569, Stuttgart, Germany*

<sup>5</sup>*E. L. Ginzton Laboratory, Stanford University, Stanford, CA, USA*

<sup>6</sup>*National Institutes for Quantum and Radiological Science and Technology, Takasaki, Gunma 370- 1292, Japan*

<sup>7</sup>*Department of Physics, Chemistry and Biology,  
Linköping University, SE-58183, Linköping, Sweden*

(Dated: April 21, 2020)

Silicon-vacancy qubits in silicon carbide (SiC) are emerging tools in quantum technology applications due to their excellent optical and spin properties. In this paper, we explore the effect of temperature and strain on these properties by focusing on the two silicon-vacancy qubits, V1 and V2, in 4H SiC. We apply density functional theory beyond the Born-Oppenheimer approximation to describe the temperature dependent mixing of electronic excited states assisted by phonons. We obtain polaronic gap around 5 and 22 meV for V1 and V2 centers, respectively, that results in significant difference in the temperature dependent dephasing and zero-field splitting of the excited states, which explains recent experimental findings. We also compute how crystal deformations affect the zero-phonon-line of these emitters. Our predictions are important ingredients in any quantum applications of these qubits sensitive to these effects.

## I. INTRODUCTION

Deep level paramagnetic point defects in solid state hosts can be utilized for quantum technology applications owing to their long living coherent spin state. In these applications, the quality of the optical properties is crucial. Additionally, these parameters are coupled to external perturbations such as changes in the strain and electromagnetic fields and temperature, either directly or elaborately mixed by spin-orbit and electron-phonon coupling. In this paper, we study these interactions in the negatively charged silicon-vacancy centers in 4H silicon carbide (SiC). These are emerging quantum defects with good spin coherence time at cryogenic temperature and fluorescence in the near infrared region<sup>1-4</sup>. The centers have  $C_{3v}$  symmetry and a spin quartet  $^4A_2$  ground state<sup>5-7</sup>. They show extremely robust zero-phonon-line (ZPL)<sup>8</sup> from the excited  $^4A_2$  state in the photoluminescence (PL) spectrum, labeled by V1 (1.438 eV) and V2 (1.352 eV) for  $h$ -site and  $k$ -site vacancy, respectively<sup>9,10</sup>. Another ZPL for  $h$ -site silicon-vacancy was observed at 5 meV higher in energy associated with the transition from the second excited  $^4E$  state called V1'<sup>6</sup>. However, its counterpart for  $k$ -site silicon-vacancy (V2') has not yet been observed. The ground and excited state spin sub-levels are split by the dipolar electron spin-electron spin interaction that is called zero-field splitting (ZFS). Due to Kramers degeneracy, only axial splitting with  $2D$  is allowed between the  $\pm\frac{1}{2}$  and  $\pm\frac{3}{2}$  levels. The experimental values of the ZFS in the ground state are 5 MHz and 70 MHz for V1 and V2 centers, respectively, that are rel-

atively small values because of the small deviation from the quasi tetrahedral symmetry of the spin density<sup>11</sup>. In striking contrast, these values are in the region of about 1 GHz in the excited state for both centers at cryogenic temperatures<sup>8,12</sup>, with a strong temperature dependence for the V2 center between the cryogenic and room temperature<sup>13</sup>.

In this paper, we wished to explore the origin of the measured magneto-optical parameters and their temperature dependence with *ab initio* calculations and experimental data. We calculated the excited state polaronic fine structure of V1 and V2 PL centers using advanced density functional theory (DFT). We modelled the vibronic interactions between these states including a crystal field strain as a perturbation. From these results, we identify V1' and V2' as polaronic excited states, in contrast with the previously assumed electronic excited states. We predict the magnitude of the ZFS in the excited state as a function of temperature. We also provide a model for the temperature dependent PL linewidth of the centers upon resonant excitation.

## II. COMPUTATIONAL METHODS

We applied a screened hybrid density functional theory, Heyd-Scuzeria-Ernzerhof HSE06 DFT<sup>14,15</sup>, for the calculation of electronic states and structure relaxation as implemented in the plane wave based Vienna Ab initio Simulation Package (VASP)<sup>16-19</sup>. This functional produces accurate ionization and excitation energies of point

defects in Group-IV semiconductors<sup>20</sup>. For the spin-orbit, vibrational and strain calculations, we used the computationally less demanding than HSE06 but still accurate Perdew-Burke-Ernzerhof (PBE) functional<sup>21</sup>. We used 420 eV plane wave cutoff and PAW formalism<sup>22</sup>. Strain calculations were carried out with an increased plane wave cutoff of 600 eV. The model of the silicon-vacancy center was embedded in a 768-atom supercell, that is sufficiently large to use  $\Gamma$ -point sampling of the Brillouin-zone. We calculated the excited electronic structure using the  $\Delta$ SCF method<sup>23</sup>. For the calculation of ZFS parameters, we used the VASP PAW<sup>24</sup> implementation of dipolar electron spin-spin interaction as implemented by Martijn Marsman. The spin quantization axis in spin-orbit coupling calculations was specified to be parallel with the symmetry axis of the defect.

### III. SAMPLE PREPARATION

The 100  $\mu\text{m}$  thick  $^{28}\text{Si}^{12}\text{C}$  isotope enriched 4H SiC layer is grown by chemical vapour deposition (CVD) on a n-type (0001) 4H SiC substrate. The isotope purity is measured by secondary ion mass spectroscopy (SIMS) and inferred to be  $^{28}\text{Si} \sim 99.85\%$  and  $^{12}\text{C} \sim 99.98\%$ . The thickness of the epitaxial layer is  $\sim 100 \mu\text{m}$  and the surface was smoothed by chemical mechanical polishing (CMP). Current-voltage measurements at room temperature shows that the layer is n-type with a free carrier concentration of  $\sim 6 \cdot 10^{13} \text{ cm}^{-3}$ , which is close to the concentration of shallow nitrogen donors of  $\sim 3.5 \cdot 10^{13} \text{ cm}^{-3}$  determined from photoluminescence at low temperatures. Deep level transient spectroscopy measurements show that the dominant electron trap in the layer is related to the carbon vacancy with a concentration in the mid  $10^{12} \text{ cm}^{-3}$  range. Minority carrier lifetime mapping of the carrier shows a homogeneous carrier lifetime of  $\sim 0.6 \mu\text{s}$ . We expect the real value to be twice as high, as an optical method with high injection was used<sup>25</sup>. Thus, the density of all electron traps should be limited to the mid  $10^{13} \text{ cm}^{-3}$  range<sup>26</sup>. Individually addressable silicon-vacancy centers were created through room temperature electron beam irradiation at 2 MeV with a fluence of  $10^{13} \text{ cm}^{-2}$ . Some interstitial-related defects were removed by subsequent annealing at 300  $^{\circ}\text{C}$  for 30 minutes. Note that the used 4H SiC sample was flipped to the side, i.e. by 90 $^{\circ}$  compared to the  $c$ -axis, such that the polarization of the excitation lasers was parallel to the  $c$ -axis ( $E \parallel c$ ) which allows to excite the V1 and V2 excited states with maximum efficiency.

To improve light extraction efficiency out of the high refractive index material ( $n \approx 2.6$ ), we fabricate a solid immersion using a focused ion beam milling machine (Helios NanoLab 650). The related surface contamination and modifications are subsequently removed by peroxy-monosulfuric acid treatment for two hours.

A thin wire is placed next to the solid immersion lens to apply continuous radiofrequency waves to mix the spin

ground states of silicon-vacancy centers. This suppresses optical spin pumping and allows for permanent observation of resonant absorption lines.

### IV. EXPERIMENTAL SETUP AND PROCEDURE

All the experiments were performed at cryogenic temperatures of 4 – 28 K in a Montana Instruments Cryostation. A home-built confocal microscope was used for optical excitation and subsequent fluorescence detection of single silicon vacancies. Initially, silicon-vacancy centers are identified via confocal microscopy and spectroscopy using continuous-wave off-resonant optical excitation at 730 nm. For resonant optical excitation at 862 nm (V1 center) we use an external cavity tunable diode laser (Toptica DLC DL PRO 850). For resonant optical excitation at 916 nm (V2 center) we use Ti:Sa laser (Msquared Solstis). All measurements are referenced to a wavelength meter (High Finesse WS7-30) with about 30 MHz accuracy.

Laser light is focused onto the sample with a vacuum-compatible microscope objective (Zeiss EC Epiplan-Neofluar 100 $\times$ , NA = 0.9). The fluorescence emission is collected by the same microscope objective and separated from parasitic laser light by a dichroic mirror (Semrock Versa Chrome Edge). Phonon side band (PSB) fluorescence is detected using a silicon single-photon counting module (Excelitas SPCM-AQRH-W4 and AQRH-14). To obtain a resonant absorption spectrum, we first apply an off-resonant laser pulse to ensure that the vacancy center is in the desired negative charge state. Then, we perform a wavelength scan with the resonant laser and infer excitation efficiency via PSB detection. Throughout all the measurement procedure, radiofrequency waves are applied continuously.

### V. THEORY

Although, we are interested in the negatively charged silicon-vacancy defect in 4H SiC, it is beneficial to start the description of the structure with its counterpart in cubic (3C) polytype. In this case, the defect has  $T_d$  point symmetry and its dangling bonds form an  $a_1$  and a  $t_2$  one-electron orbital. In the negatively charged state, five electrons occupy these states, two on the lower lying  $a_1$  orbital and three on the  $t_2$  orbital with parallel spins leading to a quartet spin ground state. The first quartet excited state can be constructed by promoting an electron from the  $a_1$  orbital to the  $t_2$  orbital in the spin minority channel. This excited state is Jahn-Teller unstable, its  $T$  orbital symmetry will be broken by  $t_2$  symmetric phonon modes ( $T \times t_2$  problem)<sup>27</sup>. The hexagonal 4H polytype produces a hexagonal crystal field which statically breaks the tetrahedral symmetry. However, the key properties of the defect can be still derived from that high sym-

metry in the cubic crystal. This crystal field is axially symmetric in 4H SiC (called the  $c$ -axis), lowering the  $T_d$  symmetry to its subgroup  $C_{3v}$ . In  $C_{3v}$ ,  $t_2$  splits to an  $a_1$  and an  $e$  orbital. Further we call the lower lying  $a_1$  orbital  $u$  and the higher one  $v$ . Analogously, the ground state configuration will result in a quartet  ${}^4A_2$ . A lower excited state can be constructed by promoting an electron from the  $u$  orbital to either the  $v$  orbital ( ${}^4A_2$ ) or the  $e$  orbital ( ${}^4E$ ). The structure of the defect and its electron configurations are depicted in Fig. 1. The fine structure of the silicon-vacancy center was determined by Soykal *et al.*<sup>28</sup>. The orbital singlets are only affected by the spin-spin interaction resulting in a splitting of the  $\pm\frac{1}{2}$  and  $\pm\frac{3}{2}$  Kramers doublets by  $2D$  (dipolar electron spin-spin interaction). In  ${}^4E$ , axial spin-orbit coupling splits  $8\times$  degeneracy (counting both the orbital and spin degeneracies) to 4 Kramers doublet levels with equal energy spacing of  $2\Delta$ . These are also affected by the spin-spin interaction analogously to the orbital singlets. The origin of vibronic coupling in this system can be still described by  $T \times t_2$  Jahn-Teller problem but in the presence of the perturbing  $C_{3v}$  crystal field. The potential energy surfaces of the  $t_2$  orbitals are formulated using pseudo-spin of three dimension. Therefore, the vibronic interaction can be expressed on this basis as a  $3 \times 3$  matrix

$$\mathbf{W} = \begin{pmatrix} 0 & -F_T Q_\zeta & -F_T Q_\eta \\ -F_T Q_\zeta & 0 & -F_T Q_\xi \\ -F_T Q_\eta & -F_T Q_\xi & 0 \end{pmatrix}, \quad (1)$$

where the orbital degrees of freedom ( $t_2^{(\xi)}$ ,  $t_2^{(\eta)}$ ,  $t_2^{(\zeta)}$ ) are depicted by the rows and columns of the  $3 \times 3$  matrix and the vibrational degrees of freedom are expressed by the  $Q_i$  configuration coordinates. The  $F_T$  linear vibronic coupling parameter connects the three  $T$  vibrational normal modes with the three  $t_2$  orbitals depicted by the matrix. The linear vibronic coupling can be expressed with the Jahn-Teller energy as follows (see Eq. (3.48) in Ref [27])

$$F_T = \sqrt{\frac{3}{2}} \hbar \omega E_{JT}. \quad (2)$$

$C_{3v}$  crystal field is introduced similarly to describe silicon-vacancies in 4H SiC. Thus the adiabatic potential energy surface (APES) on the  $t_2$  basis

$$\varepsilon(Q) = \frac{1}{2} \hbar \omega (Q_\xi^2 + Q_\eta^2 + Q_\zeta^2) \mathbf{I} + \mathbf{W} - \frac{\delta}{3} \begin{pmatrix} 0 & 1 & 1 \\ 1 & 0 & 1 \\ 1 & 1 & 0 \end{pmatrix} \quad (3)$$

consists of the phonon energy associated to the harmonic potential of the electronic APES ( $\mathbf{I}$  is the identity matrix), the vibronic interaction and the crystal field splitting ( $\delta$ ). The associated Hamiltonian describes three coupled three-dimensional harmonic oscillators

$$\hat{H} = \hbar \omega \left( \hat{a}_\xi^\dagger \hat{a}_\xi + \hat{a}_\eta^\dagger \hat{a}_\eta + \hat{a}_\zeta^\dagger \hat{a}_\zeta + \frac{3}{2} \right) \hat{I} - F \left( \hat{T}_\xi \hat{Q}_\xi + \hat{T}_\eta \hat{Q}_\eta + \hat{T}_\zeta \hat{Q}_\zeta \right) - \frac{\delta}{3} \left( \hat{T}_\xi + \hat{T}_\eta + \hat{T}_\zeta \right), \quad (4)$$

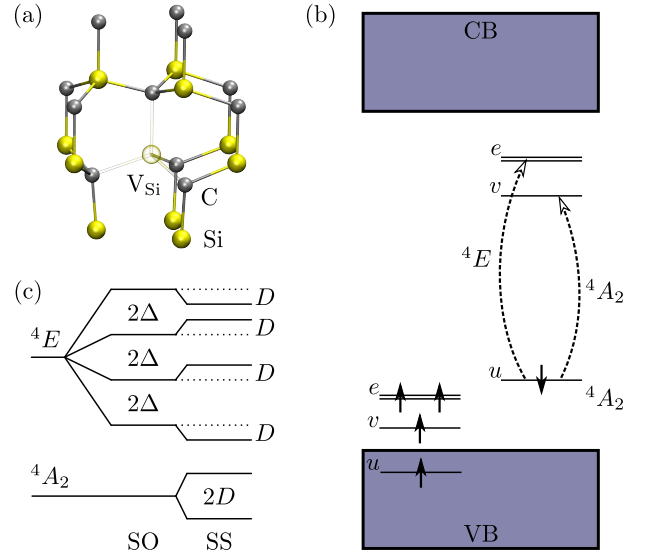


Figure 1. Geometric and electronic structure of the negatively charged silicon vacancy defect in 4H SiC. (a) Atomic model of the defect at  $h$ -site showing  $C_{3v}$  symmetry. (b) Electronic structure of the spin-polarized  ${}^4A_2$  ground state and the one-particle excitation schemes corresponding to  ${}^4A_2$  and  ${}^4E$  excited states. (c) Fine structure of the excited states regarding spin-orbit (SO) and dipolar spin-spin (SS) interactions (see Ref. 28).

where  $\hat{a}_i^\dagger$  is the  $i$  oscillator mode creation operator,  $\hat{Q}_i = \frac{1}{\sqrt{2}} (\hat{a}_i^\dagger + \hat{a}_i)$  are the coordinate operators, the pseudo-spin of  $t_2$  orbitals is represented by orbital operators

$$\hat{I} = \begin{pmatrix} 1 & 0 & 0 \\ 0 & 1 & 0 \\ 0 & 0 & 1 \end{pmatrix}, \quad \hat{T}_\xi = \begin{pmatrix} 0 & 0 & 0 \\ 0 & 0 & 1 \\ 0 & 1 & 0 \end{pmatrix}, \\ \hat{T}_\eta = \begin{pmatrix} 0 & 0 & 1 \\ 0 & 0 & 0 \\ 1 & 0 & 0 \end{pmatrix}, \quad \hat{T}_\zeta = \begin{pmatrix} 0 & 1 & 0 \\ 1 & 0 & 0 \\ 0 & 0 & 0 \end{pmatrix}. \quad (5)$$

Projections of the electronic contributions in the vibronic states to the corresponding  $a_1$  and  $e$  basis states of  $C_{3v}$  symmetry are constructed using the symmetrized combinations of the  $t_2$  orbitals.

The thermal shift and broadening of the ZPL can mainly be attributed to the vibronic interaction of quasi-degenerate orbitals, that are split by spin-orbit or crystal field interaction, with acoustic phonons. This can be modeled by time independent and time dependent perturbation theory resulting in a perturbed energy spectrum (shift) and transition rates (linewidth), respectively.

## VI. RESULTS AND DISCUSSION

### A. Polaronic spectrum in the excited state of V1 and V2 centers

We calculate the excited state relaxed structures using constrained occupation of the Kohn-Sham levels ( $\Delta$ SCF method), therefore the optical excitation is straightforwardly described by promoting an electron to an unoccupied Kohn-Sham level. The calculated ZPL energies of the  ${}^4A_2 \rightarrow {}^4A_2$  optical transition for V1 and V2 centers are 1.450 eV and 1.385 eV, respectively, are in good agreement with experimental values. However, we found the second electronic excitation ( ${}^4A_2 \rightarrow {}^4E$ ) at much larger energies, 1.792 eV and 1.953 eV, respectively. The pure electronic excitation cannot account for the observed V1' in the PL spectrum. We concluded that the observed V1' state should belong to a polaronic excited state with a mixed electronic character of  ${}^4A_2$  and  ${}^4E$ . In the following, we explore the polaronic spectrum and the vibronic mixing in these quantum bit defects to predict their magneto-optical properties as a function of temperature and strain.

We calculated the parameters in Eq. (3) with HSE06 DFT methods using a model of silicon-vacancy center in quasi- $T_d$  symmetry. As the Jahn-Teller effect originates from the occupational instability of degenerate orbitals, we can relax the system to the high symmetry configuration by "smearing" the electronic occupation of the  $a_1$  and  $e$  Kohn-Sham levels corresponding to the  $t_2$  level. The smearing eliminates the origin of symmetry breaking, thus orbital and geometric relaxation leads to the high symmetry configuration. This is done by restricting equal occupation of  $v$  and  $e$  orbitals at  $\frac{1}{3}$  in the spin minority channel. Full self-consistent solution and structural relaxation of this constraint occupation of orbitals results in the spin quartet excited state with quasi- $T_d$  geometry and wavefunctions. The remaining Kohn-Sham level splitting of  $v$  and  $e$  orbitals in this quasi- $T_d$  configuration is attributed to the  $\delta$  crystal field splitting. Jahn-Teller instability of this excited state results in a symmetry breaking of quasi- $T_d$  which leads to the two  $C_{3v}$  branches that correspond to the  ${}^4A_2$  and  ${}^4E$  excited state adiabatic potential energy surfaces (APES).

The Jahn-Teller parameters for V1 and V2 centers were calculated from the APES corresponding to quasi- $T_d \rightarrow C_{3v}$  distortion (see Table I). The calculated total energy difference of the high symmetry quasi- $T_d$  and the low symmetry  $C_{3v}$  configurations equals to  $E_{JT}$  parameter. From the high and low symmetry geometries, we calculated the normal coordinate distance of the relaxation in dimensionless units. From this result, we evaluated  $\omega$  using the harmonic approximation of the APES.  $F_T$  was obtained from Eq. (2).

We calculated the polaronic spectrum with the follow-

Table I. Jahn-Teller parameters of V1 and V2 centers obtained from DFT calculation.

center	$E_{JT}$ (meV)	$\hbar\omega$ (meV)	$\delta$ (meV)
V1	255.4	102.5	7
V2	396.5	127.5	29

Table II. Polaronic spectrum of V1 and V2 centers and the contribution of the electronic states belonging to the corresponding irreducible representation of  $C_{3v}$  point group. We define the  $|A_1\rangle\langle A_1|$ ,  $|E_x\rangle\langle E_x|$ ,  $|E_y\rangle\langle E_y|$  projectors as defined by Eq. (7) for the  $A_1$ ,  $E_x$ ,  $E_y$  contributions.

V1 center			
rel. energy (meV)	$A_1$ contr.	$E_x$ contr.	$E_y$ contr.
0.000	0.84	0.08	0.08
4.829	0.12	0.67	0.21
4.829	0.12	0.21	0.67
20.081	0.26	0.37	0.37
66.607	0.53	0.12	0.35
66.607	0.53	0.35	0.12
V2 center			
rel. energy (meV)	$A_1$ contr.	$E_x$ contr.	$E_y$ contr.
0.000	0.94	0.03	0.03
22.070	0.14	0.21	0.65
22.070	0.14	0.65	0.21
32.824	0.18	0.41	0.41
89.576	0.69	0.08	0.23
89.576	0.69	0.23	0.08

ing wavefunction Ansatz:

$$|\tilde{\Psi}\rangle = \sum_{n,m,k} \left( c_{nmk}^{(\xi)} |t_2^{(\xi)}\rangle + c_{nmk}^{(\eta)} |t_2^{(\eta)}\rangle + c_{nmk}^{(\zeta)} |t_2^{(\zeta)}\rangle \right) |n, m, k\rangle, \quad (6)$$

where we limit our phonon or vibrational expansion up to 8th order: ( $n + m + k \leq 8$ ). Thus, in other words, we limit the  $a_{\xi,\eta,\zeta}^+$  operators acting on the usual harmonic oscillator basis:  $a_n^+ |n, m, k\rangle = \sqrt{n+1} |n+1, m, k\rangle$ ,  $a_m |n, m, k\rangle = \sqrt{m-1} |n, m-1, k\rangle$ . However, the symmetry of the polaronic system is reduced from  $T_d$  thus we project out the  $A_1$  and  $E$  electronic characters of the polaronic states to  $C_{3v}$  point symmetry (see Table II) that is realized as transforming the coordinate system of Eqs. (1),(3),(5) towards the [111] direction of cubic  $T_d$  symmetry. We note that the [111] direction corresponds the  $c$  axis of 4H SiC and the two  $a$  and  $b$  depicted by the plane perpendicular to it spanned by vectors:  $[\bar{1}12]$  and  $[1\bar{1}0]$  as depicted by the equations below:

$$\begin{aligned} |A_1\rangle &= \left( |t_2^{(\xi)}\rangle + |t_2^{(\eta)}\rangle + |t_2^{(\zeta)}\rangle \right) / \sqrt{3} \\ |E_x\rangle &= \left( - |t_2^{(\xi)}\rangle - |t_2^{(\eta)}\rangle + 2|t_2^{(\zeta)}\rangle \right) / \sqrt{6} \\ |E_y\rangle &= \left( |t_2^{(\xi)}\rangle - |t_2^{(\eta)}\rangle \right) / \sqrt{2} \end{aligned} \quad (7)$$

Based on these results, we attribute the V1' ZPL line to the transition that connects the first polaronic excited

state of predominantly  $E$  electronic character to the electronic ground state. This way, the measured energy difference of V1 and V1' agrees well with the first polaronic excitation energy  $\Delta_p \sim 5$  meV. We can similarly predict its V2' counterpart to be  $\Delta_p = 22$  meV higher in energy than V2. The lack of the second sharp emission in V2 center in the experiments may be explained by the relatively large energy spacing between V2 and V2' states because V2' state could be occupied at around room temperature in the PL measurements that overlaps with the sideband of the acoustic phonon modes.

From the obtained polaronic mixing of electronic states, we determined the orientation of the optical polarization associated with V1 and V1' transition. Using the optical selection rules, optical transition between pure electronic states  $A_2 \leftrightarrow A_2$  and  $A_2 \leftrightarrow E$  is allowed by  $p_{\parallel}$  and  $p_{\perp}$  polarization, respectively.  $\parallel$  coincides with the  $c$  axis of the crystal. As V1 and V1' transitions are the polaronic mixture of the above, the observed polarization shows an inclination from  $\parallel$  direction with the angle of

$$\varphi = \arctan\left(\frac{c_A^2 \mu_A^2}{c_E^2 \mu_E^2}\right), \quad (8)$$

where  $c_A^2$  and  $c_E^2$  are the respective  $A_1$  and  $E_x + E_y$  contributions in Table II for the corresponding polaronic state.  $\mu_A^2/\mu_E^2 = 0.57$  relative transition dipole strength is obtained with the same method as discussed in Ref. 29. The resulted angles of optical polarizations from Eq. (8) are  $\varphi = 18^\circ$  and  $\varphi = 86^\circ$  for V1 and V1' transitions, respectively. These are comparable to the experimental findings of  $\sim 30^\circ$  and  $\sim 90^\circ$  in Ref. 30.

## B. Zero-field splitting in the polaronic excited state

We use HSE06 ZFS parameters of the  $^4A_2$  and  $^4E$  electronic configurations to calculate the ZFS in polaronic states as a contribution weighted average of the electronic characters. With the calculated ZFS parameters of  $2D_{^4A_2} = 1664$  MHz and  $2D_{^4E} = -1216$  MHz, the first polaronic state has  $2D = 1211$  MHz ZFS for the V1 center. Similarly, we obtain the polaronic excited state ZFS of  $2D = 1400$  MHz from  $2D_{^4A_2} = 1569$  MHz and  $2D_{^4E} = -1172$  MHz parameters for the V2 center. Here we neglected any spin-orbit interaction in the  $^4E$  excited state. The validity of this approximation is detailed later in Section VI E. We calculated the temperature dependence of ZFS for V1 and V2 centers using the Boltzmann-factor weighted average ZFS from the polaronic states at the sampling temperature values. We predict a rapid decrease for the V1 center that goes to negative values for high temperature. V2 center shows a slower transient and decrease, however, Anisimov *et al.*<sup>13</sup> measured an even more moderate slope that looks almost linear (see Fig. 2). We measured the ZFS at cryogenic temperature range using PLE. The trends here follow the DFT calculations closely. Note that the calculated values are shifted

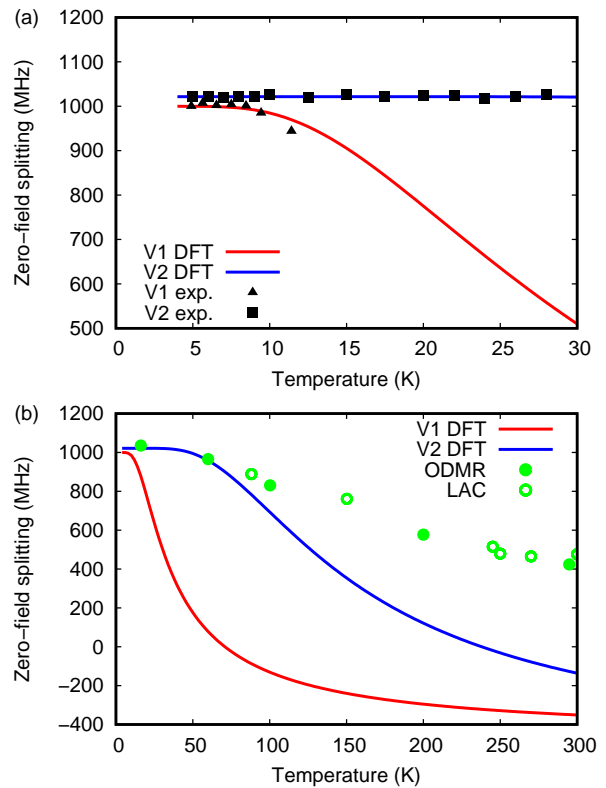


Figure 2. Temperature dependence of the excited state zero-field splitting in V1 and V2 centers (a) at cryogenic temperatures and (b) in wider temperature range. Solid curves are calculated from the Boltzmann statistics of the polaronic states with specific zero-field splitting values from the vibronic mixing. Our calculated ZFS curves are shifted by 211 MHz (V1 DFT) and 378 MHz (V2 DFT) for the sake of comparison to the tendencies of our observed PLE data in (a) and previous experimental data in (b) from Ref. 13 derived from the optically detected magnetic resonance (ODMR: solid circle) and level anticrossing (LAC: hollow circle) measurements.

in order to directly compare to the experimental data (shifting values in the caption of Fig. 2). Our DFT calculated  $D$ -parameters generally overestimate compared to the experimental ones as a consequence of spin contamination. The polaronic solution carries this systematic error as well. Furthermore, our vibronic solution relies on an effective single phonon model that cannot incorporate the features of phonon sideband with acoustic phonon modes into account. This can also result in a steeper convergence to a low ZFS in the high temperature limit. At higher temperatures, the more pronounced mixing of electronic characters should lead to an averaging to  $T_d$  symmetry where the ZFS should vanish. The experimental low and high temperature limits suggest that the intrinsic ZFS should be around 1200 MHz and  $-450$  MHz in the  $^4A_2$  and  $^4E$  excited electronic state, respectively.

### C. Temperature dependent PLE linewidth

Besides the temperature dependence of the fine structure, our polaronic solution can model the temperature dependence of the PLE linewidth as well. We expect a broadening due to the mixing of polaronic states mediated by phonons. At cryogenic temperatures, acoustic phonons dominate due to their small energy, resulting in a significant occupation number. At higher temperatures, the rapidly increasing linewidth makes the transitions between  $m_S = \pm 1/2$  and  $m_S = \pm 3/2$  indistinguishable. As the polaronic gap is quite large compared to spin-orbit splitting, we expect that only single phonon mediated processes give contribution with resonant phonon frequency to the polaronic gap. This can be formulated similarly to a resonance process in time dependent perturbation theory, where the total transition rate would be temperature dependent owing to the Bose-Einstein statistics of the acoustic phonons<sup>31</sup>. This is a temperature activated process with the specific polaronic gaps ( $\Delta_p$ ) as activation energies for V1 and V2 centers. The linewidth scales with  $\Delta_p^3$  owing to the product of linear and quadratic frequency scaling of the squared vibronic interaction strength and phonon density of states, respectively. We neglect the temperature dependence of  $\Delta_p$  that would result in a higher order correction. As  $\Delta_p$  values are much larger than the usual spin-orbit splitting of degenerate orbitals, we expect to see only the transient start of the linear dependence at cryogenic temperatures ( $T < 30$  K). Owing to the difference in the vibronic gaps, we expect the broadening of PLE lines to start at lower temperatures for the V1 center than for the V2 center. We performed temperature dependent PLE measurements for both centers (see Fig. 3) and fit the above model for the linewidth as

$$\Gamma(T) = \frac{A\Delta_p^3}{\exp\left(\frac{\Delta_p}{k_B T}\right) - 1} + \Gamma_r + \Gamma_1, \quad (9)$$

where the first fitting parameter  $A$  incorporates the average acoustic phonon density and their coupling strength.  $\Gamma_r = \frac{1}{2\pi \cdot 6 \text{ ns}}$  is the measured PL transition rate. The second fitting parameter  $\Gamma_1$  comprises all additional temperature-independent linewidth broadening processes, such as laser power broadening and spectral diffusion. Here we assume that spectral diffusion can be described by a temperature activated process with activation energy much higher than  $\Delta_p$ , thus it has negligible temperature dependence at low temperatures. The obtained parameters after this fitting procedure are summarized in Table III.

### D. Coherence of the optical emission

After consideration the dephasing of the ZPL line caused by the acoustic phonons, we turn our attention to the overall coherence of the emission. This is charac-

Table III. Fit parameters in the model of Eq. (9).

center	$A$ (GHz/meV <sup>3</sup> )	$\Gamma_1$ (GHz)
V1	$(0.37 \pm 0.03)$	$(0.065 \pm 0.004)$
V2	$(0.26 \pm 0.02)$	$(0.082 \pm 0.003)$

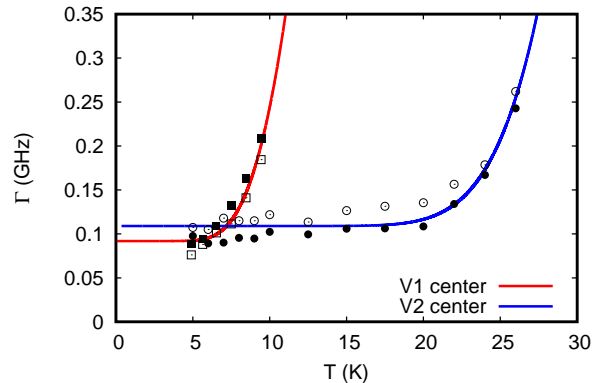


Figure 3. Temperature dependent linewidth of our observed PLE signal fit by single phonon absorption model (see Eq. (9)) to the averaged  $m_S = \pm 1/2$  (hollow points) and  $m_S = \pm 3/2$  (solid points) transitions of V1 and V2 centers.

terized by the ratio of ZPL emission in the total emission, called Debye-Waller factor. In order to study this, we measured the PL signal of the silicon-vacancy centers and calculated the phonon sideband using Huang-Rhys theory<sup>32</sup>. The high precision  $\Delta$ SCF geometry optimization enables good approximation for the phonon assisted transitions. In this method, we rely on the simplified Frank-Condon principle<sup>33,34</sup>, where we use the calculated ground state phonon spectra and normal modes. The calculation shows excellent agreement with the experimental signal (see Fig. 4). The calculated Huang-Rhys factors ( $S$ ) are relatively large at 0 K, and consequently the Debye-Waller factor is about 6% for both centers. The experimental Debye-Waller factors are about 8% and 9% for V1 and V2 centers, respectively. Note that our measured Debye-Waller factor deviates from the previously reported value<sup>4</sup>. We associate the discrepancy with the limited spectral range of the spectrometer used in the previous studies.

### E. The effect of spin-orbit coupling on the fine structure of the excited state

Next, we consider the effect of spin-orbit coupling in the  $^4E$  excited state for two reasons. Firstly, we need to estimate its contribution to the zero-field splitting in the excited polaronic state. Secondly, the intrinsic spin-orbit coupling strength is an important factor in the intersystem crossing rates towards the doublet states. Therefore, we calculated the intrinsic spin-orbit coupling strength of  $\lambda_{||} = 6\Delta = (0.29 \pm 0.04)$  meV for the V1 center and

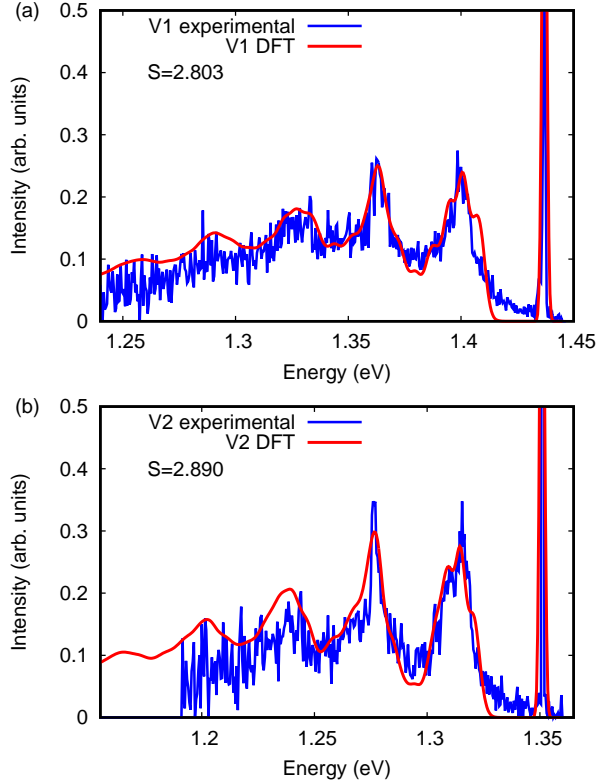


Figure 4. Experimental and calculated photoluminescence sideband of (a) V1 and (b) V2 centers. Calculated Huang-Rhys factors ( $S$ ) are shown in the figure. All experimental data are corrected for spectrometer efficiency.

$\lambda_{\parallel} = (0.41 \pm 0.04)$  meV for the V2 center by calculating the spin-orbit splitting of  $e$  Kohn-Sham orbitals in the quasi- $T_d$  excited state. These values with the corresponding standard deviation are obtained by fitting an exponential convergence for the increasing size of the supercell (see Fig. 5). The obtained strength of spin-orbit coupling is an order of magnitude smaller than the crystal field which implies that the perpendicular component of the spin-orbit coupling has a very weak contribution within second order perturbation theory. Furthermore, the parallel component can be considered as a small, independent perturbation to the electron-phonon system. By adding  $H_{SO} = \lambda_{\parallel} \mathbf{L} \mathbf{S}$  to the electron-phonon Hamiltonian in Eq. (3) we obtain 20 to 80 MHz and  $-5$  to  $-20$  MHz contribution from spin-orbit coupling to the  $D$ -parameter for V1 center in the first ( ${}^4A_2$ ) and second ( ${}^4E$ ) polaronic branches, respectively. These values are minor corrections, as they are at least an order of magnitude smaller than the original ZFS of around 1 GHz. The second polaronic excited state has  $\Delta = (3.3 \pm 1)$  GHz spin-orbit parameter which is in the expected order of magnitude<sup>35</sup>. In conclusion, the effect of spin-orbit coupling can be treated as a perturbation compared to the vibronic coupling, resulting in minor corrections in the polaronic spectrum and in the dipolar electron spin-spin

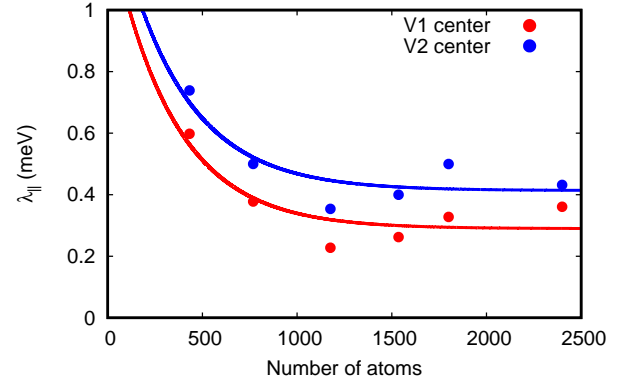


Figure 5. Size scaling of parallel spin-orbit coupling in the quasi- $T_d$  excited state configuration of V1 and V2 centers.

zero-field splitting.

#### F. Crystal strain effect on the ZPL position

The knowledge of crystal strain effects on the optical properties of the quantum defect is also an important factor in many applications, however these are yet to be measured for the  $h$  and  $k$ -site silicon-vacancy defects in 4H SiC. To determine these, we calculated the strain dependence of the ZPL position for normal strain components. We specified the strain matrix in the cubic reference frame where  $z$  and  $x$  coincides with the  $[0001]$  and  $[1\bar{1}00]$  directions in the hexagonal reference frame, respectively. This choice makes the  $(xz)$  plane a vertical mirror plane. We deformed the 4H SiC supercell according to a single strain matrix element and allowed the defect to relax under the effect of strain. We calculate the ZPL energy for a set of 7 equidistant points in the range of  $-0.003$  and  $0.003$  strain, and fit the slope ( $a$ ) to linear function. The resulting ZPL-strain coupling strengths of V1 and V2 centers are listed in Table IV.

These strain dependencies can be demonstrated in a simplified picture, where the changes in the ground state Kohn-Sham defect levels are followed. The analogy to the ZPL is the energy difference of the  $u$  and  $v$  defect level in this approximation (see Fig. 1 (b)). Compressive strain increases the charge density of the defect orbitals, leading to stronger repulsion between them, whereas the opposite can be stated for tensile strain. We find this closing tendency of the  $u$  and  $v$  energy gap in the calculations (see Fig. 6), that can be interpreted as a negative slope in the ZPL. Furthermore,  $v$  orbital is more localized on the axial carbon first neighbor of the vacancy than on the basal ones<sup>29</sup>, resulting in larger response for axial strain ( $a_{zz}$ ) compared to basal components ( $a_{xx}$  and  $a_{yy}$ ).

With piezoelectric actuators, a transverse tensile strain of up to  $7.5 \times 10^{-5}$  was already demonstrated in 4H SiC<sup>36</sup>. This could result in around  $-0.1$  meV shift in the ZPL. According to our simulations, a larger shift in ZPL can be

Table IV. Calculated ZPL-strain coupling parameters for the V1 and V2 centers in 4H SiC.

center	$a_{xx}$ (eV/strain)	$a_{yy}$ (eV/strain)	$a_{zz}$ (eV/strain)
V1	$-1.06 \pm 0.08$	$-1.41 \pm 0.03$	$-7.40 \pm 0.02$
V2	$-1.97 \pm 0.09$	$-1.89 \pm 0.07$	$-6.25 \pm 0.05$

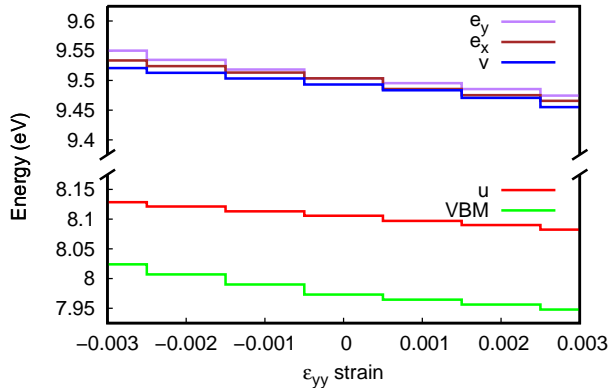


Figure 6. Strain dependence of the Kohn-Sham levels in the ground state of the V1 center. VBM is the valence band maximum,  $u$ ,  $v$  and  $e$  are the defect levels depicted in Fig. 1 (b).

obtained with applying a tensile strain parallel to  $c$ -axis. We note that pneumatical press on the sample can readily cause a large compressive strain in the order of  $10^{-3}$  that could lead to several meVs shift of the ZPL transitions. This strong coupling to strain can be harnessed in quantum communication applications, where identical emitters are needed for efficient coupling of distant qubits with photons. An efficient control of the ZPL position compensating local differences (e.g., temperature) could be achieved by applying a specific strain using piezo actuators.

## VII. CONCLUSION

We investigated the negatively charged silicon-vacancy defects in 4H SiC at the hexagonal and cubic site, called V1 and V2 PL centers. We take electron-phonon interaction into account to describe their magneto-optical properties and their coupling to external perturbations. We represent this interaction based on the quasi-tetrahedral symmetry of the defect that is lowered by the crystal field of the host. We accurately reproduce the V1' level as a

vibronic excited state and predict the V2' counterpart. We predict the temperature dependence of the optical linewidth and zero-field splitting that show different features for the two defects. We also determined the normal strain dependence of the ZPL position in the order of magnitude at eV/strain. Finally, we obtained the intrinsic spin-orbit coupling parameters about 0.3 and 0.4 meV for V1 and V2 centers, respectively, that does not contribute to the temperature dependence but are important in understanding the intersystem crossing processes.

The physics of the vibronic coupling in the excited state is closely related to quantum applications, notably those requiring emission of highly indistinguishable photons. This comprises distribution of remote entanglement via photonic interference in a quantum repeater network<sup>37</sup>, and generation of photonic cluster states for measurement-based quantum computation<sup>38,39</sup>. The discussed interaction process with phonons in the excited state is directly related to the rate of pure dephasing of a single photon state, which affects the photon indistinguishability<sup>40</sup>. Further, strain tuning of the ZPL emission, as discussed in this work, can provide an efficient means to match the photon emission wavelengths of multiple defects, or to tune emitters into resonances of optical cavities for improving photon emission rates.

## ACKNOWLEDGEMENT

A.G. acknowledges the National Excellence Program of Quantum-Coherent Materials Project (Hungarian NKFIH Grant No. KKP129866), the EU QuantERA Q-Magine Project (Grant No. 127889), the QuantERA Nanospin Project (Grant No. 127902), the EU H2020 Quantum Technology flagship project ASTERIQS (Grant No. 820394), and the National Quantum Technology Program (Grant No. 2017-1.2.1-NKP-2017-00001). J.W. thanks the Max Planck Society as well as the EU via the ERC project SmEL. N.T.S. acknowledges the Swedish Research Council (Grant No. VR 2016-04068), J.U.H. thanks the Swedish Energy Agency (43611-1), N.T.S. and J.U.H. thank the Knut and Alice Wallenberg Foundation (Grant No. KAW 2018.0071). A.G., N.T.S. and J.U.H. thank the EU H2020 project QuanTELCO (Grant No. 862721). T.O. thanks the Japan Society for the Promotion of Science (Grant No. JSPS KAKENHI 17H01056 and 18H03770). J.V. acknowledges the US Department of Energy, Office of Science, under award No. DE-SC0019174. The computations were performed on resources provided by the Swedish National Infrastructure for Computing (SNIC) at NSC.

<sup>1</sup> Pavel G. Baranov, Anna P. Bundakova, Alexandra A. Soltamova, Sergei B. Orlinskii, Igor V. Borovykh, Rob Zondervan, Rogier Verberk, and Jan Schmidt, “Silicon vacancy in sic as a promising quantum system for single-

defect and single-photon spectroscopy,” *Phys. Rev. B* **83**, 125203 (2011).

<sup>2</sup> T. C. Hain, F. Fuchs, V. A. Soltamov, P. G. Baranov, G. V. Astakhov, T. Hertel, and V. Dyakonov, “Excitation and



- recombination dynamics of vacancy-related spin centers in silicon carbide,” *Journal of Applied Physics* **115**, 133508 (2014), <https://doi.org/10.1063/1.4870456>.
- 3 Matthias Widmann, Sang-Yun Lee, Torsten Rendler, Nguyen Tien Son, Helmut Fedder, Seoyoung Paik, Li-Ping Yang, Nan Zhao, Sen Yang, Ian Booker, Andrej Denisenko, Mohammad Jamali, S. Ali Momenzadeh, Ilja Gerhardt, Takeshi Ohshima, Adam Gali, Erik Janzén, and Jörg Wrachtrup, “Coherent control of single spins in silicon carbide at room temperature,” *Nature Materials* **14**, 164–168 (2015).
  - 4 Roland Nagy, Matthias Widmann, Matthias Niethammer, Durga B. R. Dasari, Ilja Gerhardt, Öney O. Soykal, Marina Radulaski, Takeshi Ohshima, Jelena Vučković, Nguyen Tien Son, Ivan G. Ivanov, Sophia E. Economou, Cristian Bonato, Sang-Yun Lee, and Jörg Wrachtrup, “Quantum properties of dichroic silicon vacancies in silicon carbide,” *Phys. Rev. Applied* **9**, 034022 (2018).
  - 5 N. Mizuochi, S. Yamasaki, H. Takizawa, N. Morishita, T. Ohshima, H. Itoh, T. Umeda, and J. Isoya, “Spin multiplicity and charge state of a silicon vacancy ( $T_{V2a}$ ) in 4h-sic determined by pulsed EPR,” *Phys. Rev. B* **72**, 235208 (2005).
  - 6 Erik Janzén, Adam Gali, Patrick Carlsson, Andreas Gällström, Björn Magnusson, and N.T. Son, “The silicon vacancy in sic,” *Physica B: Condensed Matter* **404**, 4354 – 4358 (2009).
  - 7 H. Kraus, V. A. Soltamov, D. Riedel, S. Väh, F. Fuchs, A. Sperlich, P. G. Baranov, V. Dyakonov, and G. V. Astakhov, “Room-temperature quantum microwave emitters based on spin defects in silicon carbide,” *Nature Physics* **10**, 157 EP – (2013), article.
  - 8 Roland Nagy, Matthias Niethammer, Matthias Widmann, Yu-Chen Chen, Péter Udvarhelyi, Cristian Bonato, Jawad Ul Hassan, Robin Karhu, Ivan G. Ivanov, Nguyen Tien Son, Jeronimo R. Maze, Takeshi Ohshima, Öney O. Soykal, Ádám Gali, Sang-Yun Lee, Florian Kaiser, and Jörg Wrachtrup, “High-fidelity spin and optical control of single silicon-vacancy centres in silicon carbide,” *Nature Communications* **10** (2019), 10.1038/s41467-019-09873-9.
  - 9 Mt. Wagner, B. Magnusson, W. M. Chen, E. Janzén, E. Sörman, C. Hallin, and J. L. Lindström, “Electronic structure of the neutral silicon vacancy in 4h and 6h sic,” *Phys. Rev. B* **62**, 16555–16560 (2000).
  - 10 Viktor Ivády, Joel Davidsson, Nguyen Tien Son, Takeshi Ohshima, Igor A. Abrikosov, and Adam Gali, “Identification of si-vacancy related room-temperature qubits in 4h silicon carbide,” *Phys. Rev. B* **96**, 161114 (2017).
  - 11 Nguyen Tien Son, Pontus Stenberg, Valdas Jokubavicius, Takeshi Ohshima, Jawad Ul Hassan, and Ivan G Ivanov, “Ligand hyperfine interactions at silicon vacancies in 4h-SiC,” *Journal of Physics: Condensed Matter* **31**, 195501 (2019).
  - 12 Hunter B. Banks, Öney O. Soykal, Rachael L. Myers-Ward, D. Kurt Gaskill, T.L. Reinecke, and Samuel G. Carter, “Resonant optical spin initialization and readout of single silicon vacancies in 4h-SiC,” *Phys. Rev. Applied* **11**, 024013 (2019).
  - 13 A. Anisimov, Dmitriy Simin, V. Soltamov, S. Lebedev, Pavel Baranov, G. Astakhov, and V. Dyakonov, “Optical thermometry based on level anticrossing in silicon carbide,” *Scientific Reports* **6** (2016), 10.1038/srep33301.
  - 14 Jochen Heyd, Gustavo E. Scuseria, and Matthias Ernzerhof, “Hybrid functionals based on a screened coulomb potential,” *The Journal of Chemical Physics* **118**, 8207 (2003).
  - 15 Aliaksandr V. Krukau, Oleg A. Vydrov, Artur F. Izmaylov, and Gustavo E. Scuseria, “Influence of the exchange screening parameter on the performance of screened hybrid functionals,” *The Journal of Chemical Physics* **125**, 224106 (2006).
  - 16 G. Kresse and J. Hafner, “*Ab initio* molecular dynamics for liquid metals,” *Phys. Rev. B* **47**, 558–561 (1993).
  - 17 G. Kresse and J. Furthmüller, “Efficient iterative schemes for *ab initio* total-energy calculations using a plane-wave basis set,” *Phys. Rev. B* **54**, 11169–11186 (1996).
  - 18 G. Kresse and J. Furthmüller, “Efficiency of *ab-initio* total energy calculations for metals and semiconductors using a plane-wave basis set,” *Computational Materials Science* **6**, 15 – 50 (1996).
  - 19 J. Paier, M. Marsman, K. Hummer, G. Kresse, I. C. Gerber, and J. G. Ángyán, “Screened hybrid density functionals applied to solids,” *The Journal of Chemical Physics* **124**, 154709 (2006).
  - 20 Peter Deák, Bálint Aradi, Thomas Frauenheim, Erik Janzén, and Adam Gali, “Accurate defect levels obtained from the hse06 range-separated hybrid functional,” *Phys. Rev. B* **81**, 153203 (2010).
  - 21 John P. Perdew, Kieron Burke, and Matthias Ernzerhof, “Generalized gradient approximation made simple,” *Phys. Rev. Lett.* **77**, 3865–3868 (1996).
  - 22 P. E. Blöchl, “Projector augmented-wave method,” *Phys. Rev. B* **50**, 17953–17979 (1994).
  - 23 Adam Gali, Erik Janzén, Péter Deák, Georg Kresse, and Efthimios Kaxiras, “Theory of spin-conserving excitation of the  $n - V^-$  center in diamond,” *Phys. Rev. Lett.* **103**, 186404 (2009).
  - 24 Zoltán Bodrog and Adam Gali, “The spin-spin zero-field splitting tensor in the projector-augmented-wave method,” *Journal of Physics: Condensed Matter* **26**, 015305 (2014).
  - 25 Tsunenobu Kimoto and James A. Cooper, *Fundamentals of Silicon Carbide Technology* (John Wiley & Sons, 2014).
  - 26 Katsunori Danno, Daisuke Nakamura, and Tsunenobu Kimoto, “Investigation of carrier lifetime in 4h-sic epilayers and lifetime control by electron irradiation,” *Applied Physics Letters* **90**, 202109 (2007).
  - 27 Isaac Bersuker, *The Jahn-Teller Effect* (Cambridge University Press, 2006).
  - 28 Ö. O. Soykal, Pratibha Dev, and Sophia E. Economou, “Silicon vacancy center in 4h-sic: Electronic structure and spin-photon interfaces,” *Phys. Rev. B* **93**, 081207 (2016).
  - 29 Péter Udvarhelyi, Roland Nagy, Florian Kaiser, Sang-Yun Lee, Jörg Wrachtrup, and Adam Gali, “Spectrally stable defect qubits with no inversion symmetry for robust spin-to-photon interface,” *Phys. Rev. Applied* **11**, 044022 (2019).
  - 30 David O. Bracher, Xingyu Zhang, and Evelyn L. Hu, “Selective purcell enhancement of two closely linked zero-phonon transitions of a silicon carbide color center,” *Proceedings of the National Academy of Sciences* **114**, 4060–4065 (2017), <https://www.pnas.org/content/114/16/4060.full.pdf>.
  - 31 Kay D Jahnke, Alp Sipahigil, Jan M Binder, Marcus W Doherty, Mathias Metsch, Lachlan J Rogers, Neil B Manson, Mikhail D Lukin, and Fedor Jelezko, “Elec-

- tron–phonon processes of the silicon-vacancy centre in diamond,” *New Journal of Physics* **17**, 043011 (2015).
- <sup>32</sup> Kun Huang, Avril Rhys, and Nevill Francis Mott, “Theory of light absorption and non-radiative transitions in F-centres,” *Proceedings of the Royal Society of London. Series A. Mathematical and Physical Sciences* **204**, 406–423 (1950), <https://royalsocietypublishing.org/doi/pdf/10.1098/rspa.1950.0184>.
- <sup>33</sup> Audrius Alkauskas, Bob B Buckley, David D Awschalom, and Chris G Van de Walle, “First-principles theory of the luminescence lineshape for the triplet transition in diamond NV centres,” *New Journal of Physics* **16**, 073026 (2014).
- <sup>34</sup> Adam Gali, Tamás Demján, Márton Vörös, Gergo Thiering, Elena Cannuccia, and Andrea Marini, “Electron-vibration coupling induced renormalization in the photoemission spectrum of diamondoids,” *Nature Communications* **7**, 11327 (2016).
- <sup>35</sup> Sophia E Economou and Pratibha Dev, “Spin-photon entanglement interfaces in silicon carbide defect centers,” *Nanotechnology* **27**, 504001 (2016).
- <sup>36</sup> Abram L. Falk, Paul V. Klimov, Bob B. Buckley, Viktor Ivády, Igor A. Abrikosov, Greg Calusine, William F. Koehl, Adam Gali, and David D. Awschalom, “Electrically and mechanically tunable electron spins in silicon carbide color centers,” *Phys. Rev. Lett.* **112**, 187601 (2014).
- <sup>37</sup> Peter C. Humphreys, Norbert Kalb, Jaco P. J. Morits, Raymond N. Schouten, Raymond F. L. Vermeulen, Daniel J. Twitchen, Matthew Markham, and Ronald Hanson, “Deterministic delivery of remote entanglement on a quantum network,” *Nature* **558**, 268–273 (2018).
- <sup>38</sup> I. Schwartz, D. Cogan, E. R. Schmidgall, Y. Don, and D. Gershoni, “Deterministic generation of a cluster state of entangled photons,” *Science* **354**, 434–437 (2016), <https://science.sciencemag.org/content/354/6311/434.full.pdf>.
- <sup>39</sup> Rui Vasconcelos, Sarah Reisenbauer, Cameron Salter, Georg Wachter, Daniel Wirtitsch, Jörg Schmiedmayer, Philip Walther, and Michael Trupke, “Scalable spin-photon entanglement by time-to-polarization conversion,” *npj Quantum Information* **6**, 9 (2020).
- <sup>40</sup> Naoya Morioka, Charles Babin, Roland Nagy, Izel Gediz, Erik Hesselmeier, Di Liu, Matthew Joliffe, Matthias Niethammer, Durga Dasari, Vadim Vorobyov, Roman Kolesov, Rainer Stöhr, Jawad Ul-Hassan, Nguyen Tien Son, Takeshi Ohshima, Péter Udvarhelyi, Gergő Thiering, Adam Gali, Jörg Wrachtrup, and Florian Kaiser, “Spin-controlled generation of indistinguishable and distinguishable photons from silicon vacancy centres in silicon carbide,” (2020), arXiv:2001.02455 [quant-ph].